INVESTIGATION OF THE DUCTED-PROPELLER EFFECTS ON AEROACOUSTIC PERFORMANCE USING PHASE-LOCKED PIV

Jianwei Sun, Chiba University, Chiba, Japan
Koichi Yonezawa, Central Research Institute of Electrical Power Industry, Abiko, Japan
Hao Liu, Chiba University, Chiba, Japan

Abstract

This paper presents an integrated study of the aerodynamic and acoustic performance of a shrouded/ducted propeller, with a specific focus on unveiling the underlying mechanisms associated with the aeroacoustic interplay between the duct and propeller. Using phase-locked particle image velocimetry (PIV), we examined three cases: ducted propellers at relative distances of d = 0.11r, d = 0.29r, and a non-ducted propeller. The integrated analysis combining PIV measurements and numerical simulations unveils noise variation mechanisms. Our findings demonstrate that a shift in the duct-propeller relative position from d = 0.29r to d = 0.11r can reduce overall sound pressure levels by an average of 5.5 dB. The attenuation in noise is attributed to the maintained integrity of tip vortices and increased diffusion of trailing edge vortex sheets at d = 0.11r. The duct's inlet lip preserves tip vortices, thereby decreasing pressure fluctuations and limiting trailing edge noise.

1. INTRODUCTION

Quadrotor drones, a type of unmanned aerial vehicle (UAV) or micro air vehicle (MAV) capable of vertical takeoff and landing (VTOL), have a wide range of civilian applications, including surveillance, aerial mapping, and delivery (Ref. 1). Due to their convenience, low cost, and simple maneuverability, they have attracted growing attention from both industrial and academic researchers. One key area of focus is optimizing the propulsion system for improved aerodynamic and aeroacoustic performance.1

Ducted propellers offer a highly efficient and safe propulsion solution for quadrotor drones by reducing the slipstream contraction, increasing the overall thrust, and suppressing vortex shedding (reducing induced drag). Previous studies (Refs. 2, 3, and 4) have shown that the propeller-duct interaction has a significant impact on the aerodynamic and aeroacoustic performance of ducted propellers. Pereira (Ref. 4) studied the hover performance systematically and found that compared to non-ducted propellers, the ducted propeller achieved a 94% increase in thrust at the same power consumption and a 62% reduction in power consumption. However, the aeroacoustic issue, i.e., the noise of the propulsion system, remains a challenging topic. In our previous study (Ref. 3), we found that the aerodynamic and acoustic characteristics of the ducted propeller are significantly dependent on the relative propeller-duct location. We observed a 10 dB fluctuation in overall sound pressure level (OASPL) associated with broadband noise and a significant improvement (55%) in thrust coefficients at d = 0.23r in the middle of the duct diffuser.

Despite the many previous studies focused on the aerodynamic and aeroacoustic performance of ducted propellers, the interplay between the propeller and the duct that affects the noise emission remains poorly understood. This study aims to address this gap by conducting an integrated study of the propeller-duct-induced aeroacoustic interaction using both PIV measurements and CFD-based simulations. The results of this study show how the location adjustment of the ducted propeller can alter the tip vortices and trailing edge vortex sheet and thus affect the noise emission of the ducted propeller.

2. EXPERIMENTAL SETUPS AND CFD MODELING

2.1. Aerodynamic and acoustic measurements

Aerodynamic (thrust and torque) and acoustic measurements were made through a hover-stand experiment in an anechoic chamber at Chiba University's Nishi Chiba Campus. The room's internal dimensions were 3.86 m long, 1.56 m wide, and 2.4 m high. As depicted in Figure 1, the acoustic characteristics associated with ducted propellers were measured by using a hover stand test in an anechoic chamber, with a microphone array mounted in an arc-shaped rail of a radius of 500 mm (R) at four polar angles (θ) of 0 deg, 25 deg, 50 deg, and 75 deg. The propeller has a rotor radius (r) of 100 mm with a tip clearance of 1.5 mm (0.015 r) and a rotational speed of 5517 RPM. The duct has a length (L) of 36 mm, with an arc-shaped inlet lip section (blue) of a radius of 15 mm and a straight section (green) of 21 mm long. The distance (d) between inlet lip leading edge and propeller rotational plane varied from -55 mm to 105 mm. Detailed experimental setup can be found in our previous study (Ref. 3).

2.2. PIV experimental setups

The particle image velocimetry (PIV) was conducted with a hover-stand experiment in a wind tunnel at Chiba University's Nishi Chiba Campus. The tunnel's test section of dimensions was 2 m long, 1 m wide, and 1 m high. The facility is described by Ref. 5 where the PIV system consists of a diode-pumped solid-state laser (DSSPL) system (532nm, 2W, SANZ, Japan), high-speed camera (FASTCAM Mini AX50, Photron inc., Japan), 8-channel timing controller (LC800, LabSmith inc., USA), and pulse output tachometer (FT3406, HIOKI co., Japan). The flow is seeded with particles produced by a PIVpart14 (PIVTEC – GmbH, Göttingen, Germany) with around 1 µm of diameter. The tracer particles are recirculated in the wind tunnel to ensure uniform mixing before the experiment. The high-speed camera of 1024 pixels × 560 pixels resolution captured the PIV images by the rate of 4,000 frames per second (fps) by the exposure time of 1/10,000 sec. The calculation of PIV measurements was conducted in four passes. The first interrogation area was 128 pixels in length with a step of 32 pixels, while length of 64 pixels with step of 32 pixels in pass 2. The third interrogation area was 32 pixels in length with a step of 16 pixels, while length of 16 pixels with step of 8 pixels in pass 4. All the PIV measurements is

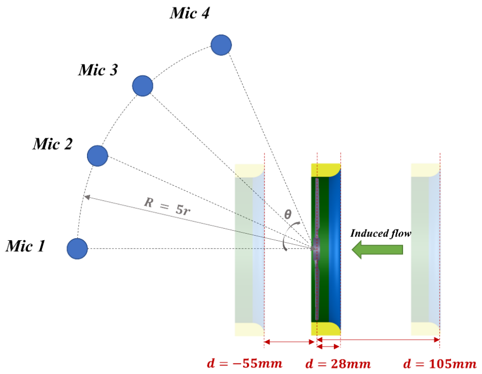

(a) Schematic of a setup for acoustic measurement

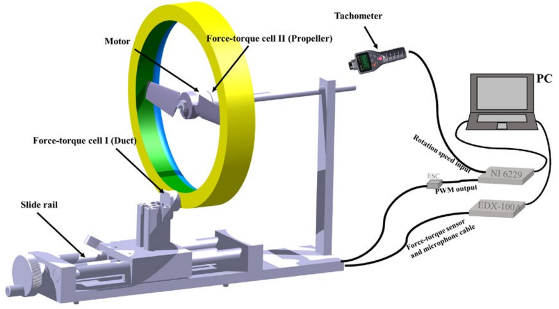

(b) Schematic of a setup for aerodynamic measurement

Figure 1: Experimental setups for acoustic (a) and aerodynamic (b) measurements of a ducted propeller.

calculated by PIVlab (Ref. 6) with the fast Fourier transform window deformation algorithm, standard correlation robustness and the Gaussian 2x3 point estimator for sub-pixel movement.

To carry out the periodic and detailed flow structure at specific phase angles, we developed a phase-locked PIV measurement system which can take a pair of PIV images at specific phase angles using synchronized signal generated by timing controller. As shown in Figure 2, the Mini AX50 was triggered by delayed digital signal from tachometer and capture pair images at 4,000 fps which is used to calculate the instantaneous velocity at certain phase angles. First delayed digital signal (delay 1) was used to acquire phase-locked PIV measurements at different certain phase angles. The second delayed digital signal (delay 2) was used to add a delayed time between pairwise PIV images for the instantaneous velocity calculation. In this study, the

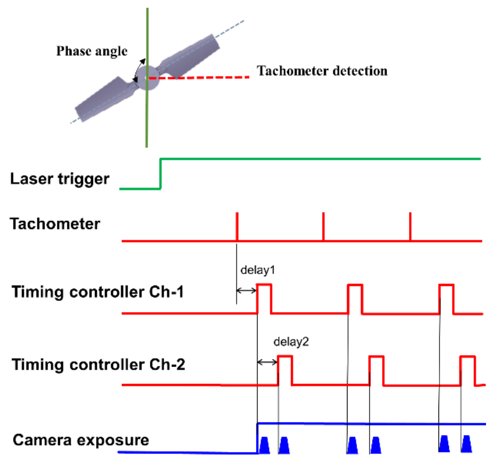

(a) Signal system for phase-locked PIV measurement

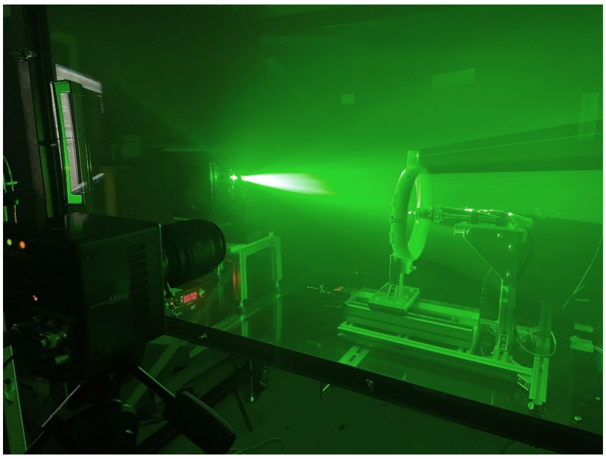

(b) Photograph of the setup for PIV measurement

Figure 2: Experimental setups for PIV measurements.

instantaneous velocities were measured at the 12 specific locked-phase angles range from 0 deg to 330 deg with 30 deg increments by adjustment of delayed time in LC800. Each phase-averaged result was calculated based on 2000 frames of instantaneous field measurement. Generic PIV measurements (free-run) were also conducted to calculate the time-averaged result. The time-averaged flow field of free-run measurements were calculated via 4,000 PIV images i.e., 2,000 PIV instantaneous result frames.

2.3. CFD Modeling

To quantify the flow structures around the ducted propeller and examine the aerodynamic interplay between the duct and the propeller, we further carried out a series of CFD-based simulations using an

Grid	Grid points
Background grid	449 x 449x 313 ($X \times Y \times Z$)
Duct grid	119 x 167x51 ($circumferential \times$ height $\times normal$)
Each blade grid	105x 71 x 41 (span $\times chord \times normal$)

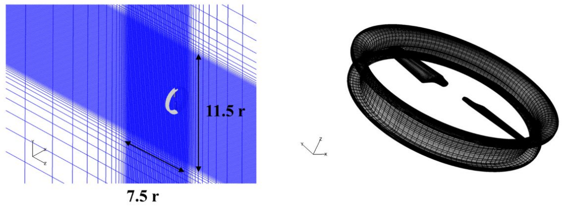

Figure 3: Computational domain and grids of a ducted propeller.

inhouse CFD solver of the NS (Navier–Stokes equations), which is a computer code called rFlow3D developed by JAXA, specified for the computations of unsteady incompressible flows around a rotorcraft in a manner of multi-blocked domain and overlapped grids. The simulations here were conducted under the conditions of a rotational speed of 5400 rpm for the ducted propeller model with d = 0.29 r and d = 0.11 r, respectively. A benchmark test was already performed associated with the verification of the CFD solver and the validation of rotorcrafts in our previous studies (Ref. 3). In this study, the grids as shown in Figure 3 comprise three body-fitted blocks of the blade grid, the duct grid, and the background grid. The refined inner background dimensions 11.5r × 11.5r × 7.5r; the rotational speed was set to be 5400 rpm for each blade with duct. The computed pressures were nondimensionalized as pressure coefficient (C_{pa}), such as:

(1) $$C_{pa} = \frac{\tilde{p}-p_\infty}{\frac{1}{2}\rho a_\infty^2},$$

where a_∞ is speed of sound, $\tilde{p}$ is local pressure of the flow field, p_∞ is far field pressure, and ρ is air density. The time-averaging and phase-averaging operations based on instantaneous velocity were calculated by

(2) $$\hat{v} = \frac{1}{N}\sum_{i=1}^{N} v(t_0 + i\,\Delta t),$$

$$\bar{v} = \frac{1}{N}\sum_{i=1}^{N} v(t_0 + i\,T),$$

where $\hat{v}$ is the time-dependent velocity, t_0 is the stating time which depends on the phase angle in phase-averaging operations, N is the number of samples, Δt is the size of time step, and T is the period of a propeller revolution. All simulations were performed until the flow fields converged to reach a stable state.

3. RESULT

3.1. Aerodynamic and Acoustics Performance

The result of aerodynamic and aeroacoustic performance was presented in our previous study (Ref. 3). In this study, the experimental and numerical investigation of ducted propeller flow field were conducted at the d = 0.11r and d = 0.29r as well as non-ducted propeller, where the averaged OASPL at the distance of 5r is 67.2dB, 73.6dB, and 68.5dB; the overall coefficient of thrust is 0.016, 0.017 and 0.010, respectively.

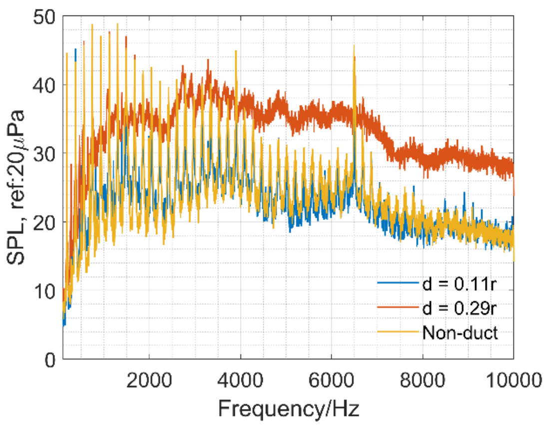

Figure 4: Power spectral densities of the ducted propeller at d = 0.11r, d = 0.29r, and non-ducted propeller observed at Mic 1 (θ =0 deg).

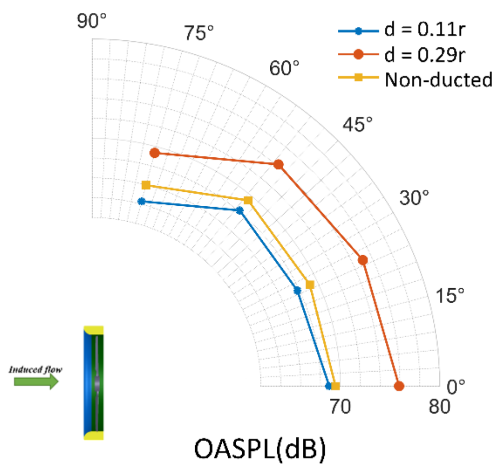

Figure 5: Comparison of OASPL (dB) distributions at microphone array for ducted propeller at d = 0.29 r, d = 0.11 r, and non-ducted propeller.

3.2. Flow Structure Visualization

The main flow features of the ducted propeller model were visualized by phase-averaged velocity based on the instantaneous velocities by PIV measurements and CFD simulation. Contours of the phase-averaged velocities in Z component normalized by the tip speed of rotational propeller are illustrated in Figure 6 for the ducted propeller at d = 0.11 r, d = 0.29r, and non-ducted propeller, where the result of PIV and CFD are generally in good agreement. In order to investigate the flow structure of tip vortices and trailing edge vortex, the vortices fields of ducted propeller calculated by arithmetic averages of instantaneous vorticities obtained from phase-locked PIV measurement at 0 deg of phase angles were illustrated in Figure 7. The vorticities are normalized by the period of one propeller revolution. For the case of non-ducted propeller, the tip vortices having strong negative vorticity is a major identifiable feature which is a typical wake of finite wing because of the pressure difference between pressure side and suction side. The tip vortices of wake age 540 deg roll up with wake age 720 deg and merge with it. It is worthy to note that the shape and integrity of tip vortices was partially or completely interacted for the ducted propeller model at d = 0.11 r and d = 0.29 r as shown in Figure 7. Moreover, the trailing edge vortex sheets, generated by the flow passing the trailing edge of the propeller, can be visible with positive vorticity in both cases of ducted and non-ducted propeller. The vortex sheet seen in these cases was previously observed by Ramasamy (Ref. 7) using smoke flow visualization. It is worth noting that the trailing edge vortex sheets downwashes faster than the tip vortices since they were generated simultaneously in the non-ducted case. As a result, the vortex sheet will merge and break down with the tip vortices generated from another blade at the previous cycles, for example, the trailing edge vortex sheet of wake age 360 deg interact and merge with the tip vortices of wake age 540 deg and 720 deg in the non-ducted case. Therefore, only three vortex sheets were shown with six tip vortices in the case of non-ducted propeller in Figure 7 (c). The ducted propeller at d = 0.11r generated the larger tip vortices and weak trailing edge vortex sheets compared to non-ducted propeller, whereas the ducted propeller at d = 0.29r generated the completely broken-up tip vortices and more trailing edge vortex sheets, as shown in Figure 7. Additionally, with respect to aeroacoustics, through the visualized

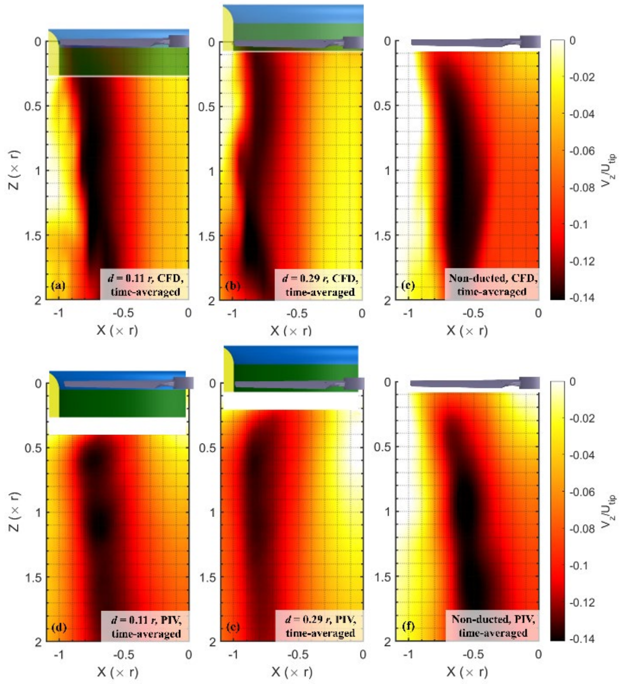

Figure 6: Comparison of contours of time-averaged velocities normalized by the tip velocity between PIV measurements (d, e, f) and CFD results (a, b, c) of the ducted propeller at d = 0.11r: (a, d), d = 0.29r: (b, e), and non-ducted propeller (c, f).

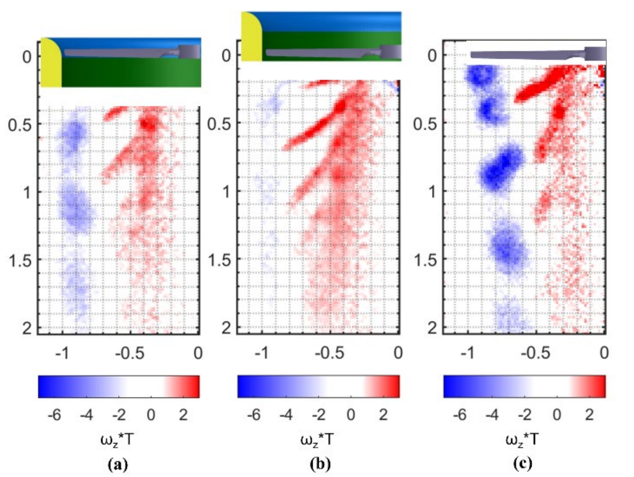

Figure 7: Vorticity distributions of the Phase-locked PIV measurement results at 0 deg of phase angle: ducted propeller at d = 0.11r (a), d = 0.29r (b), and non-ducted propeller (c)

root mean square (rms) of pressure coefficient distributions in Figure 8, the pressure fluctuation shows the significant discrepancy of non-ducted propeller and ducted propeller model at d = 0.11r and d =

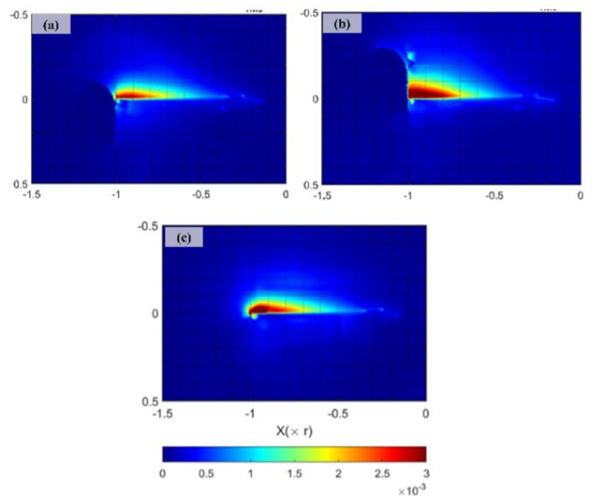

Figure 8: Contours of pressure fluctuations coefficient (P_{rms}) around ducted propeller models at d = 0.11r (a) and d = 0.29r (b), and non-ducted propeller (c).

0.29r. It is obvious that the ducted propeller model at d = 0.11 r reduces the pressure fluctuation remarkably, which is in good agreement with the result of acoustic measurement in Figure 4.

4. DISCUSSION

Here we investigate how the duct-propeller axial position affect the noise variance with a focus on tip vortices and trailing edge vortex sheet as well as their interaction.

In the case of ducted propeller at d = 0.29r where the propeller disc is vicinity to outlet of duct, the tip vortices are completely broken up to the smaller eddies as the new sound source of broadband noise which supports the result by the Ref. 2. The distributions of root mean square (rms) of the pressure fluctuations in Figure 8(b) further demonstrate that the interaction between duct and propeller suppress the formation of tip vortices increase the pressure fluctuation in the suction zone at d = 0.29 r. In contrast, the inlet lip and the propeller offer the zone to generate the tip vortices reducing the pressure fluctuation (Figure 8(a)) on the upper surface of the ducted propeller model at d = 0.11 r where propeller disc is on the inlet lip of duct. The tip vortices generated by ducted propeller model at d = 0.11r maintain shedding like that non-ducted propeller and further develop a large size vortex as shown in the Figure 7(a). To investigate the tip vortices shedding of the ducted propeller model at d = 0.11 r, we conducted the phase-locked PIV measurement by close-up

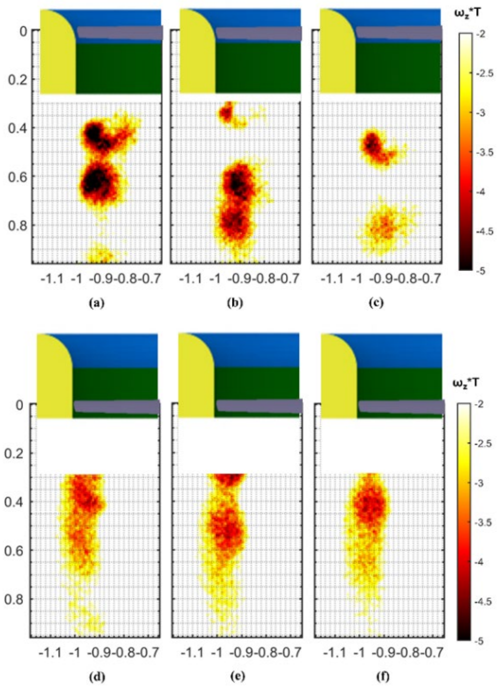

Figure 9: Vorticity distributions of the Phase-locked PIV measurement results for ducted-propeller model at d = 0.11r (a-c) and d = 0.29r (d-f): 0 deg (a, d), 120 deg (b, e), and 240deg (c, f) of phase angle.

view to achieve the higher resolution in vorticity field (Figure 9). The zoom-in vorticity field indicates the tip vortices generated by the ducted propeller model at d = 0.11 r roll up and merge with the wake age 180 deg vortex and form a larger vortex with two vortex cores at around H = 0.5 r (Figure 9(a-c)). Whereas the tip vortices of ducted propeller model at d = 0.29 r were completely broken up by the interaction with the wall of duct, which are seen as small eddies chaotically (Figure 9(d-f)). This implies that at the straight section (d = 0.15 r – 0.36 r) the interaction between propeller and duct broke up tip vortices to small eddies which increase the broadband noise significantly as the experimental result in anechoic chamber, whereas the ducted-propeller model at d = 0.11r remains the tip vortices structure owing to the inlet lip.

5. CONCLUSIONS

In this study we present an integrated study of the propeller-duct-induced aeroacoustic interaction by combining PIV measurements and CFD-based simulations to examine the mechanism of noise variance. The results show that when the relative position between the duct and the propeller is changed from d = 0.29r to d = 0.11r, the OASPL can be reduced by approximately 5.5 dB on average. The PIV results indicate that the noise reduction is likely due to the integrity of the tip vortices at the relative position of d = 0.11r together with the enhanced diffusion of the trailing edge vortex sheet at d = 0.11r. The inlet lip of the duct can avoid a remarked break-up of the tip vortices, thus reducing pressure fluctuations while suppressing trailing edge noise. Future work may be conducted the PIV measurements at various flight conditions to explore the validity and underlying aeroacoustic mechanisms. Additionally, the findings of this study can provide a useful design of low-noise propeller-duct systems for drones, as well as for other aircrafts.

Author contact:

Jianwei Sun sunjianwei@chiba-u.jp

Koichi Yonezawa koichi-y@criepi.denken.or.jp

Hao Liu hliu@faculty.chiba-u.jp

6. ACKNOWLEDGMENTS

This work is partially supported by the Grant-in-Aid for Scientific Research of KAKENHI No. 19H00750, JSPS, and the Centre for Aerial Intelligent Vehicle (CAIV), Graduate School of Engineering, Chiba University.

7. REFERENCES

1. Floreano, Dario, and Robert J. Wood. "Science, technology and the future of small autonomous drones." nature 521.7553 (2015): 460-466.
2. Malgoezar, Anwar MN, Ana Vieira, Mirjam Snellen, Dick G. Simons, and Leo LM Veldhuis. "Experimental characterization of noise radiation from a ducted propeller of an unmanned aerial vehicle." International Journal of Aeroacoustics 18, no. 4-5 (2019): 372-391.
3. Sun, Jianwei, Koichi Yonezawa, and Hao Liu. "Experimental Investigation of Aeroacoustic Interaction between Propeller and Duct." In 28th AIAA/CEAS Aeroacoustics 2022 Conference, p. 3033. 2022.
4. Pereira, Jason L. Hover and wind-tunnel testing of shrouded rotors for improved micro air vehicle design. University of Maryland, College Park, 2008.
5. Ikeda, Teruaki, Tetsuya Ueda, Toshiyuki Nakata, Ryusuke Noda, Hiroto Tanaka, Takeo Fujii,

and Hao Liu. "Morphology effects of leading-edge serrations on aerodynamic force production: An integrated study using PIV and force measurements." Journal of Bionic Engineering 15 (2018): 661-672.

6. Thielicke, William, and René Sonntag. "Particle Image Velocimetry for MATLAB: Accuracy and enhanced algorithms in PIVlab." *Journal of Open Research Software* 9.1 (2021).

7. Ramasamy, Manikandan, Timothy E. Lee, and J. Gordon Leishman. "Flowfield of a rotating-wing micro air vehicle." Journal of aircraft 44, no. 4 (2007): 1236-1244.